

Research Article

Numerical Investigation of the Combustion in an Improved Microcombustion Chamber with Rib

Hai Chen  and Wei-qiang Liu

College of Aerospace Science and Engineering, National University of Defense Technology, Changsha 410073, China

Correspondence should be addressed to Hai Chen; chfair@163.com

Received 26 July 2019; Revised 27 September 2019; Accepted 12 October 2019; Published 22 November 2019

Guest Editor: Jiaqiang E

Copyright © 2019 Hai Chen and Wei-qiang Liu. This is an open access article distributed under the Creative Commons Attribution License, which permits unrestricted use, distribution, and reproduction in any medium, provided the original work is properly cited.

This study proposes an improved microcombustor with a rectangular rib to improve the temperature level of the combustor wall. Moreover, the OH mass fraction, temperature distribution, and outer wall temperature of the original and improved combustors of premixed hydrogen/air flames are numerically investigated under various inlet velocities and equivalence ratios. Results show that the improved microcombustor enhances heat transfer between the mixture and wall because its recirculation zone is larger than that of the original, thereby resulting in high wall temperature. Conversely, thermal resistance in the horizontal direction increases with upstream and downstream step lengths. Consequently, the outer wall temperature decreases with step length in the improved combustor. A high equivalence ratio (e.g., 0.6) may result in the destruction of the combustor because the wall temperature has exceeded the acceptable temperature of wall material quartz. Therefore, the improved microcombustor is recommended for micro-thermo-photovoltaic systems.

1. Introduction

Micro-electro-mechanical system (MEMS) technology has received considerable attention in recent years [1–3]. Micro-power generation devices based on combustion has several advantages, such as light weight, high-power density, long charge duration, and short recharging time [4–6]. Thus, micro-power generation devices are deemed suitable alternatives to conventional batteries. Moreover, these devices can be applied in micro fuel cells, micro gas turbines, and micro-thermo-electric, and thermo-photovoltaic systems [7, 8].

A micro-thermophotovoltaic (TPV) system geometry consists of photovoltaic cells, emitter, filter, and heat source (Figure 1). A microcombustor is a core part of the micro-TPV system, in which the chemical energy of the fuel is converted into other energy through combustion. Hence, research on microcombustor with a large operation range has received increasing attention. However, the short residence time of mixtures and high heat loss due to the high surface area-to-volume ratio of the microcombustor result

in flame instability and low blow-off limit [9–11]. Therefore, enhancing flame stability and extending the operating range present significant issues. By using structure design to form a low-velocity zone or recirculation zone, the flame stability and combustion performance of the microcombustor can be improved.

Peng et al. [12] numerically examined the thermal performance of a microcombustion chamber with and without a front cavity and found that the front cavity enhances the stability of the microcombustor. Wan et al. [13–16] numerically investigated the behavior of an H₂/air blend in a microcombustion chamber with cavities and found that recirculation and low-velocity zones are formed in the concave cavity. The flame is unstable in the combustor without cavities but can be effectively stabilized in a combustor with cavities. These cavities can also expand the working range of the inlet velocity. Bagheri et al. [17] numerically studied the combustion characteristics of premixed hydrogen/air in microcombustors with different bluff body structures (e.g., semicircular, ellipse, half ellipse, wall-blade, and arrowhead) at different inlet velocities and found

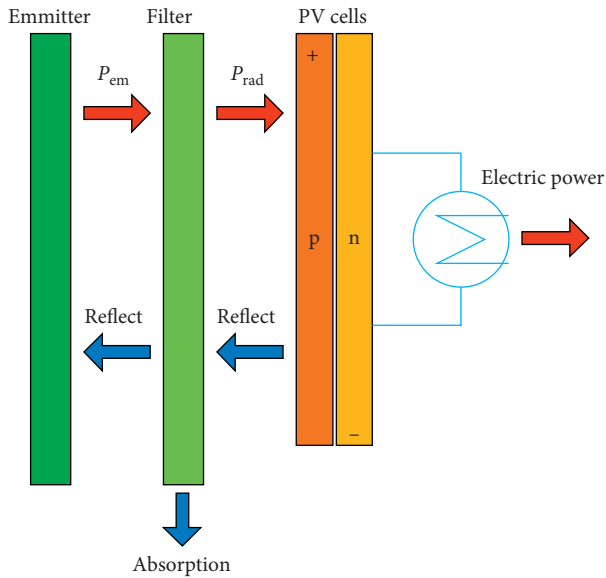


FIGURE 1: Energy conversion process of a micro-thermophotovoltaic (TPV) system.

that the combustion chamber with a wall fin as a bluff body shows the highest flame temperature and emission efficiency when the inlet velocity is 10 m/s. Jiaqiang et al. [18] established a methane/air premixed combustion model in a microcombustor and found that the combustion performance is improved at a 45° backward-facing step angle, a quartz wall material, an inlet velocity ranging from 2 m/s to 4 m/s, and a high field synergy. Zuo et al. [19] proposed a microcylindrical combustion chamber with a rib and numerically investigated the behavior of microcombustors. They found that the outer wall temperature of the improved combustion chamber is higher and more uniform than that of the microcombustion chamber without a rib. Wan et al. [20] designed a microcombustor with a flat flame stabilizer and two preheating channels and found that the blowout limit of the combustor initially increases and then decreases along with an increasing plate length. Jiaqiang et al. [21] found that the inlet pipe structure of the combustor improves the mixing performance of H_2/O_2 and enhances flame stabilization and heat recirculation by using a backward-facing step and cavity. Yilmaz et al. [22, 23] established a combined structure of cavity, poststage, and microchannel in a combustor and then studied its combustion characteristics. They found that the average wall temperature, wall temperature distribution, and combustion efficiency of the new combustor have been significantly improved. Zuo et al. [24] designed a counterflow double-channel microcombustion chamber in which the inner diameter of the combustor gradually increases. They found that the improved combustor has a more uniform and a much higher wall temperature compared with the combustor with a backward-facing step. Yan et al. [25] numerically analyzed the behavior of methane/air in a microcombustion chamber with a regular triangular pyramid bluff body and found that the blow-off limit of the improved microcombustor is nearly twice larger than that of the original microcombustor. Ansari and

Amani [26] numerically examined a novel planar microcombustion chamber with a combined bluff and baffle structure for micro-TPV systems and found that this new combustor outperforms a combustor with only one baffle or cylinder in terms of flame stability and combustion efficiency. Li et al. [27] numerically studied the effects of channel height and inlet velocity on combustion characteristics in a 2D planar microcombustion chamber with a separating plate and found that the mixing effect can be improved by reducing the inlet velocity and channel height. Tang et al. [28] numerically and experimentally studied the propane/air premixed combustion performance of a new cross-plate microplanar combustor and found that the cross-plate enhances the heat transfer and increases the average wall temperature by more than 90 K. The new structure also extended the blowout limit of the cross-plate combustor. Zuo et al. [29] found that the efficiency and emission power of the microelliptical combustor are 2.17% and 0.68 W higher than those of the microcircular tube combustor when the long axis-short axis ratio and hydrogen mass flow rate are 1.9/1.18 and 7×10^{-7} kg/s, respectively. Akhtar et al. [30] found that the outer wall temperature of the curved groove combustor increases by 110 K and that the energy conversion rate increases by 7.84% compared with the straight groove. Aravind et al. [31] proposed a three-backward-facing-step microcombustion chamber with a recirculation hole and added a porous medium (ceramic cotton) to the combustion chamber. They found that the porous media preheat the mixture through a thermal cycle and that the flame stability is significantly improved.

The use of a catalyst on the surface of a microcombustion chamber can reduce the activation energy required for the ignition of mixed gas and improve the combustion efficiency and stability of the combustion chamber.

Li and Hong [32] added hydrogen to methane fuel by using a platinum tube with a perforated ring to improve the combustion stability and radiation intensity of the microthermoelectric system of the combustion chamber. They found that the effective power efficiency of the TPV system is 3.24%. Yan et al. [33] performed a numerical simulation of platinum catalytic combustion on a microplate combustor for methane/air catalytic combustion. They found that a low inlet velocity can increase methane conversion, but a high-temperature region can easily be formed near the inlet. Therefore, preheating the mixed gas by using a wall material with high thermal conductivity is necessary. Ran et al. [34] conducted numerical studies on the characteristics of methane catalytic combustion in a microcombustion chamber with a convex cavity and a combustion chamber without a cavity. The results showed that the methane conversion increases and then decreases with the increase in equivalence ratio. When the equivalence ratio equals 1, the conversion rate of methane in the convex wall cavity reaches the maximum at 85.3%. The convex cavity microcombustion chamber reaches the highest flameout limit at 16.5 m/s. Luo et al. [35] used the $Pd/Al_2O_3/Fe-Ni$ catalyst to perform catalytic combustion experiments on low-concentration methane in a microcombustion chamber; they analyzed the effects of flow rate, methane concentration, and burner

temperature on the methane conversion rate. The results showed that temperature is the most critical factor affecting conversion. Pan et al. [36] investigated the catalytic combustion process of premixed methane/air in a rectangular microcombustion chamber via experimentation. The outer wall temperature distribution and the main components of flue gas were measured separately. The results indicated that the addition of platinum to the microcombustion chamber significantly improves the combustion stability of the microchannel. After platinum is added to the combustion chamber, the outer wall temperature becomes further uniform and the methane conversion rate is increased. Rodrigues et al. [37] explored the methane/air catalytic combustion of microcombustion chambers with cobalt oxide (CO_3O_4) as coating. They found that methane is completely burned at a temperature of 760°C . When the temperature is lower than 600°C , only the catalytic reaction will occur in the combustion chamber. However, when the temperature is above 600°C , the combustion chamber will simultaneously produce the gas phase and catalytic combustion. Moreover, CO_3O_4 has remarkable application potential. Wang et al. [38] investigated the catalytic combustion of methane and *n*-butane in microtubes with Pt/ZSM-5 as the catalyst via experimentation. The results showed that the stable combustion range of *n*-butane is slightly higher than that of methane. When *n*-butane is used as fuel, the penetrating wall of the combustion chamber has a high heat loss rate and temperature. *n*-butane can be used as an alternative fuel to methane when necessary.

Although a combustor wall temperature level that is sufficiently high is desired for thermoelectric and thermophotovoltaic devices, such a level is difficult to achieve because heat loss increases substantially with the surface area-to-volume ratio of the microcombustor. Furthermore, the residence time of the mixture decreases when the combustion chamber is scaled down. Thus, cavities are included into a planar microcombustor [13–16]. Moreover, the effect of cavity geometry on combustion performance is evaluated. In contrast to previous studies, we improved a microcombustor through the application of a rib on the basis of the literature [13–16]. Thereafter, the current study numerically investigates the combustion performance of the improved microcombustor under various inlet velocities and equivalence ratios.

2. Mathematical-Physical Model of a Combustor

2.1. Physical Model of a Microcombustor. The schematic diagram of a ribless microcombustion chamber is presented in Figure 2. The cavity length (L_2) and total length (L_0) of the microcombustion chamber are 3.0 mm and 18.0 mm, respectively. The thickness of the combustion chamber walls (W_3) is 2 mm. The height (W_1) and width (W_0) of the combustor chamber are 1 mm and 10 mm, respectively. The depth (W_2) and length (L_1) of the cavities are 1 mm and 3 mm, respectively. In contrast to the original combustion chamber in Figure 2(a), a rib is added into the cavity, as shown in Figure 2(b). The rib width is 0.5mm. The rib

heights (H), upstream (L_3), and downstream (L_4) step lengths are various. The improved microcombustion chamber with various step lengths and rib heights are shown in Table 1.

2.2. Modeling Equations. The characteristic scale of the microcombustion chamber is substantially larger than the molecular mean-free path of blends. Therefore, the gas mixture is regarded as continuous [13–16].

Kuo and Ronney found that the realizable k-epsilon model is optimal in calculating the combustion performance compared with the laminar model because the Reynolds number is above or approximately 500 [39]. In this study, the Reynolds number exceeds 500 because the inlet velocity is either equal to or over 10 m/s in the improved combustor. In addition, the laminar finite rate model is optimal compared with the other model. Hence, this research adopts the realizable k-epsilon model and laminar finite rate model for the numerical simulation. Moreover, a two-dimensional steady-state model was employed because of the large aspect ratio ($W_0/W_1 = 10:1$) of the microcombustion chamber.

Continuity equation is given as follows:

$$\frac{\partial(\bar{v}_x + v'_x)}{\partial x} + \frac{\partial(\bar{v}_y + v'_y)}{\partial y} = 0. \quad (1)$$

The momentum equation is given as follows:

$$\frac{\partial(\rho\bar{v}_i\bar{v}_j)}{\partial x_j} = -\frac{\partial\bar{p}}{\partial x_i} + \frac{\partial}{\partial x_j} \left(\eta \frac{\partial\bar{u}_i}{\partial x_j} - \rho u'_i u'_j \right). \quad (2)$$

The energy equation is given as follows:

$$\begin{aligned} \frac{\partial(\rho v_x C_p T)}{\partial x} + \frac{\partial(\rho v_y C_p T)}{\partial y} &= \frac{\partial((\lambda_f + \lambda_{ft})\partial T)}{\partial x^2} \\ &+ \frac{\partial((\lambda_f + \lambda_{ft})\partial T)}{\partial y^2} + \sum_i \left[\frac{\partial}{\partial x} \left(C_{p,i} T \rho D_{m,i} \frac{\partial Y_i}{\partial x} \right) \right. \\ &\left. + \frac{\partial}{\partial y} \left(C_{p,i} T \rho D_{m,i} \frac{\partial Y_i}{\partial y} \right) \right] + \sum_i C_{p,i} T R_i. \end{aligned} \quad (3)$$

The species equation is given as follows:

$$\frac{\partial(\rho Y_i v_x)}{\partial x} + \frac{\partial(\rho Y_i v_y)}{\partial y} = \frac{\partial}{\partial x} \left(\rho D_{m,i} \frac{\partial Y_i}{\partial x} \right) + \frac{\partial}{\partial y} \left(\rho D_{m,i} \frac{\partial Y_i}{\partial y} \right) + R_i, \quad (4)$$

where $C_{p,i}$, R_i , and Y_i denote specific heat capacity, generation or consumption rate, and the mass fraction of species i , separately; while λ_{ft} and λ_f are turbulent thermal conductivity and thermal conductivity of the blends, separately.

2.3. Computation Scheme. The mass, momentum, energy, and species conservation equations are solved using Fluent. The density of the gas blends is calculated using the ideal gas assumption, while the specific heat is determined using the mixing law. Kinetic theory is used for the blend mass diffusivity, while the mass-weighted mixing law is adopted to calculate the

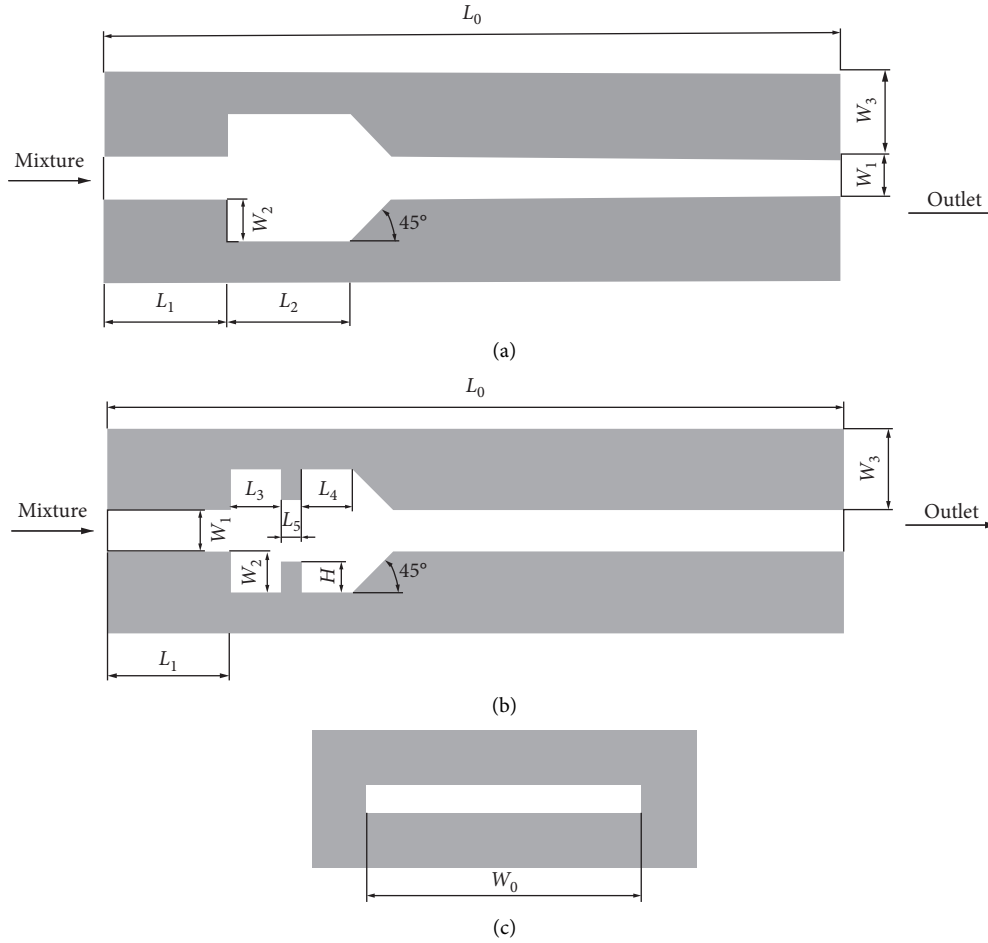


FIGURE 2: Schematic diagram of the microcombustor: (a) without rib, (b) with rib, and (c) combustor exit.

TABLE 1: The improved microcombustion chamber with various step lengths and rib heights.

	Upstream step lengths (L_3) (mm)	Downstream step lengths (L_4) (mm)	Rib heights (H) (mm)
Case A	1.25	1.25	0.75
Case B	2.25	1.25	0.75
Case C	3.25	1.25	0.75
Case D	1.25	2.25	0.75
Case E	1.25	3.25	0.75
Case F	1.25	1.25	0.25
Case G	1.25	1.25	0.55

thermal conductivity and viscosity of the gas mixture. The COUPLED algorithm and the second-order upwind scheme were selected to couple the pressure and velocity. “Temperature patches” of 2000 K and 1350 K on the fluid and solid zones, respectively, were used to ignite the H_2 /air mixture.

This study adopts the chemical kinetic mechanism of the H_2 reaction reported in Li et al. [40], which comprises 13 species and 19 reversible elementary reactions. Wan et al. [13–16] verified the chemical mechanism by simulating the combustion of H_2 /air. The simulated results were compared with the experimental results reported in the literature [41]. Accordingly, the numerical results are consistent with the experimental data.

The boundary conditions are as follows. The velocity condition was specified at the inlet, whereas the pressure outlet condition was adopted at the outlet. The nonslip boundary condition was adopted in the simulation. The inlet temperature of the microcombustor was fixed at 300 K. Quartz was used as the solid material. The specific heat capacity, density, and thermal conductivity of the quartz material were 750 J/kg/K, 2650 kg/m³, and 1.05 W/m/K, respectively.

The heat loss in the solid wall immensely influences the combustion. Therefore, the heat transfer in the channel walls is considered in the numerical simulation. The heat loss on the exterior surfaces includes radiation, while natural convection is computed as follows:

TABLE 2: Calculation results of the different grid spacings in the two-dimensional structure of a microcombustor.

Grid spacing (m)	Exhausted gas temperature (K)	Mean outer wall temperature (K)	Mass fraction of hydrogen at the outlet (%)
1×10^{-5}	1197.1	1037.5	0.001930354
2×10^{-5}	1197.01	1037.7	0.001931158
3.3×10^{-5}	1195.2	1041.5	0.002078265
4×10^{-5}	1195	1043.5	0.002161413

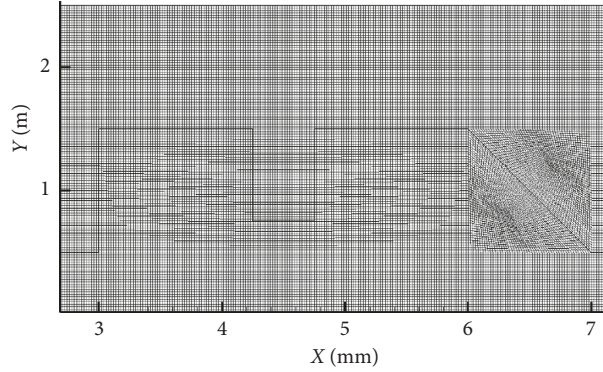


FIGURE 3: Demonstration of the grid system near the upper cavity.

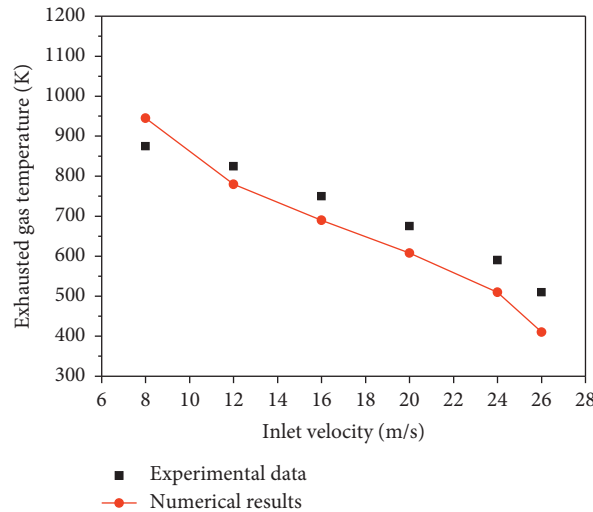


FIGURE 4: Comparison between experimental data and numerical results for exhaust gas temperature in the original microcombustor.

$$q = h_0(T_w - T_\infty) + \varepsilon\sigma(T_w^4 - T_\infty^4), \quad (5)$$

where h_0 is the natural convection heat transfer coefficient, $20 \text{ W}/(\text{m}^2\text{K})$, T_w is the exterior wall temperature, ε is the interior and exterior emissivity of solid surface with a value of 0.92, T_∞ is the ambient temperature (300 K), and σ is the Stephan–Boltzmann constant $5.67 \times 10^{-8} \text{ W}/\text{m}^2/\text{K}^4$.

2.4. Grid Independence. A grid correlation test was conducted with a two-dimensional model of the original microcombustion chamber under four mesh intervals: 1×10^{-5} , 2×10^{-5} , 3.3×10^{-5} , and 4×10^{-5} m, as shown in Table 2. The inlet velocity and equivalence ratios of the simulation case were equal to 10 m/s and 0.4, respectively; the heat transfer coefficient was $20 \text{ W}/\text{m}^2/\text{K}$; and the radiation emissivity of the outer wall was 0.92 [13–16]. The

results showed that the hydrogen at the outlet and temperature differences for the four-grid spacing were minimal. Furthermore, the difference was not obvious when grid spacing was equal to 1×10^{-5} and 2×10^{-5} m. Thus, the grid spacing of 2×10^{-5} m was deemed sufficient to achieve high accuracy in a short computation time for the numerical investigation. The numerical model of the microcombustor was meshed using approximately 227600 structured cells, as shown in Figure 3.

2.5. Model Verification. We compared the numerical results of the exhausted gas temperature on the original model with the experimental data in the literature [13–16], as shown in Figure 4. The results of the numerical model and the model in the literature [13–16] shared the same changing trend. The maximum temperature difference was 98 K. This result

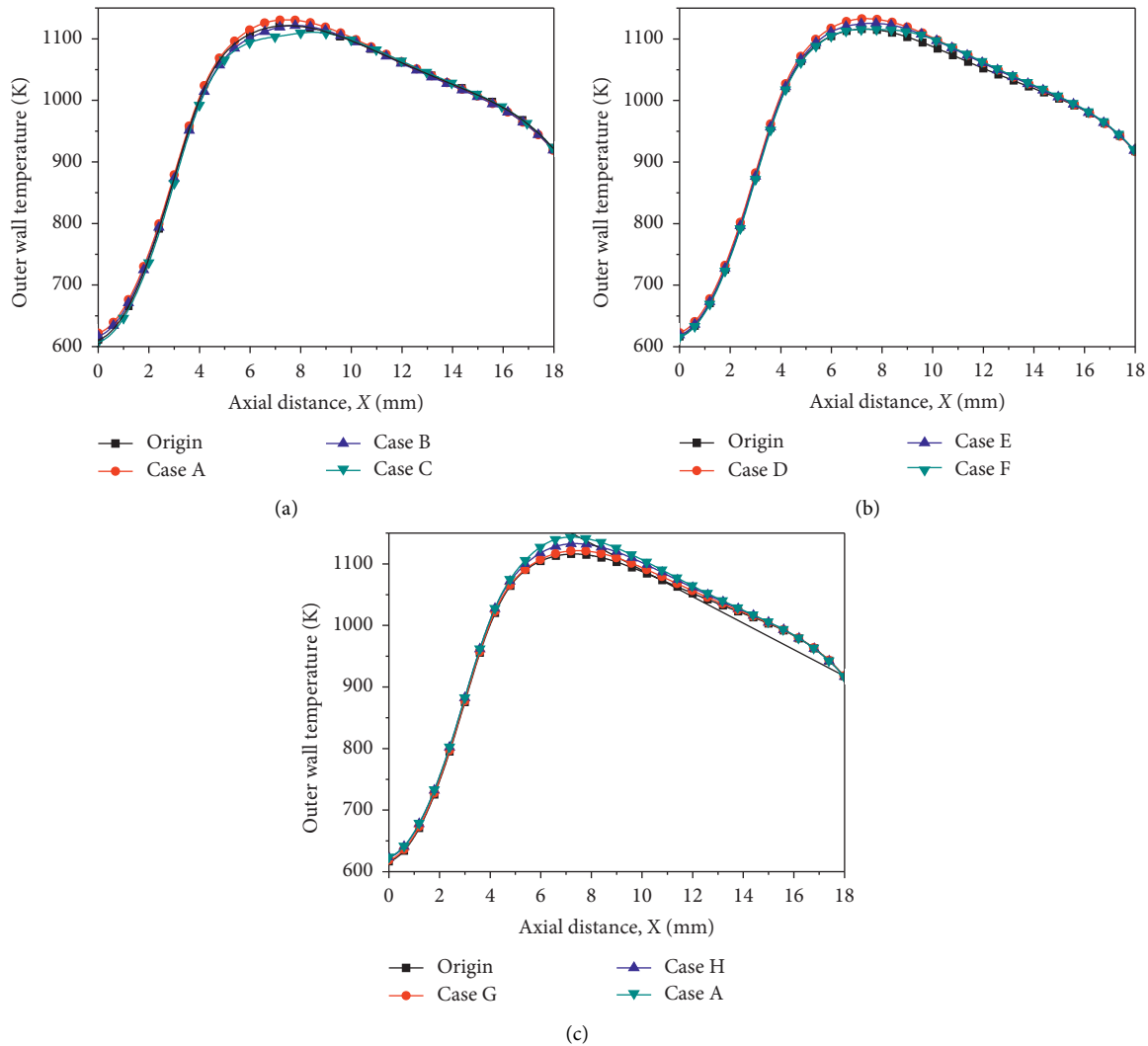


FIGURE 5: Outer wall temperature profiles for the original and improved combustor with inlet velocity equal to 10 m/s.

confirmed the numerical model is reliable to research the combustion performance in the microcombustion chamber.

3. Results and Discussions

3.1. Effects of Rib Position on Combustion Characteristics. We plot the outer wall temperature profiles for the different microcombustors (Figure 5). The lengths of the rib and upstream and downstream steps vary. This figure shows that the outer wall temperature profile increases from the inlet and reaches a peak around the center of the cavity. Thereafter, the temperature profile descends with further increase in the axis length because of heat losses from the outer wall. Figures 5(a) and 5(b) show that the outer wall temperature profile of the combustor becomes inverted against the upstream and downstream step lengths. This result is caused by an increase in the thermal resistance in the horizontal direction because of the thinning outer wall of the cavity. Hence, low heat is conducted upstream through the thin outer wall with a large right-step length. Moreover, the outer wall temperature level increases with an increase in the

rib height (Figure 5(c)). The newly proposed combustor has a higher wall temperature than that of the original.

The contours of the longitudinal velocity component near the cavities at inlet velocities of 10 m/s are presented in Figure 6 to clarify the mechanism by which the newly proposed combustor improves the wall temperature level. The equivalence ratio is maintained at 0.4. The region where the longitudinal velocity is below 0 is considered the recirculation zone, where as that where such a velocity is between 0 and 10 m/s is considered the low-velocity zone. Figure 6 shows that the recirculation zones of the microcombustion chamber with a rectangular rib are divided into two parts, in which the area of the recirculation zone of the microcombustion chamber with the rib is larger than that without the rib. This feature enhances heat transfer between the blends and inner walls, while the residence time of the mixture is also prolonged. Thus, the outer wall temperature of the improved combustor is higher than that of the original combustor. The recirculation zone area is nearly maintained because the upstream and downstream step lengths are approximately 2.25 mm.

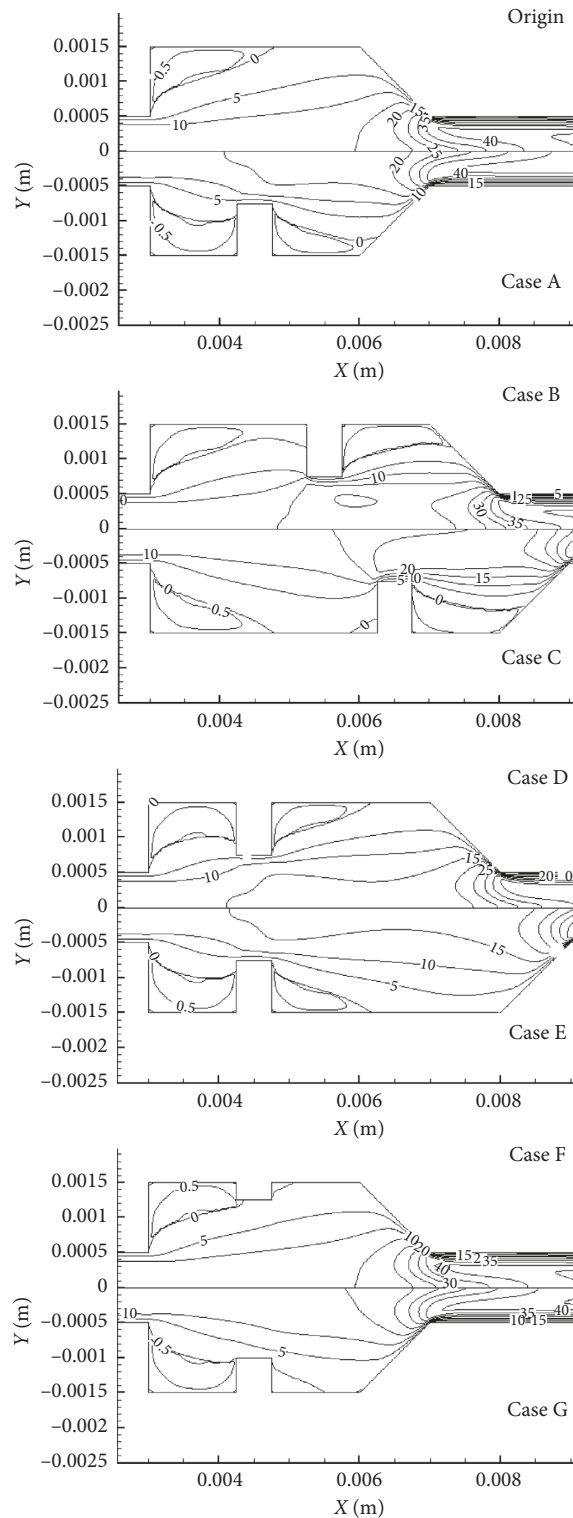


FIGURE 6: Contours of the longitudinal velocity component in the region near the cavities. The inlet velocity is 10 m/s.

Figure 7 presents the average wall temperatures of the different microcombustion chambers with and without the rib under different inlet velocities. Accordingly, the equivalence ratio is maintained at 0.4. Figures 7(a) and 7(b) show that the average wall temperature increases with the inlet velocity, which is below 32 m/s. The mean outer wall temperature decreases with the continuous increase in inlet

velocity because of the short residence time in the combustor. Among the studied microcombustors, the average wall temperature of the combustion chamber with $L_3 = 1.25$ mm and $L_4 = 1.25$ mm is the highest when the inlet velocity is kept constant. Given the increase in upstream and downstream step lengths, the corresponding mean outer wall temperature decreases owing to the increase in thermal

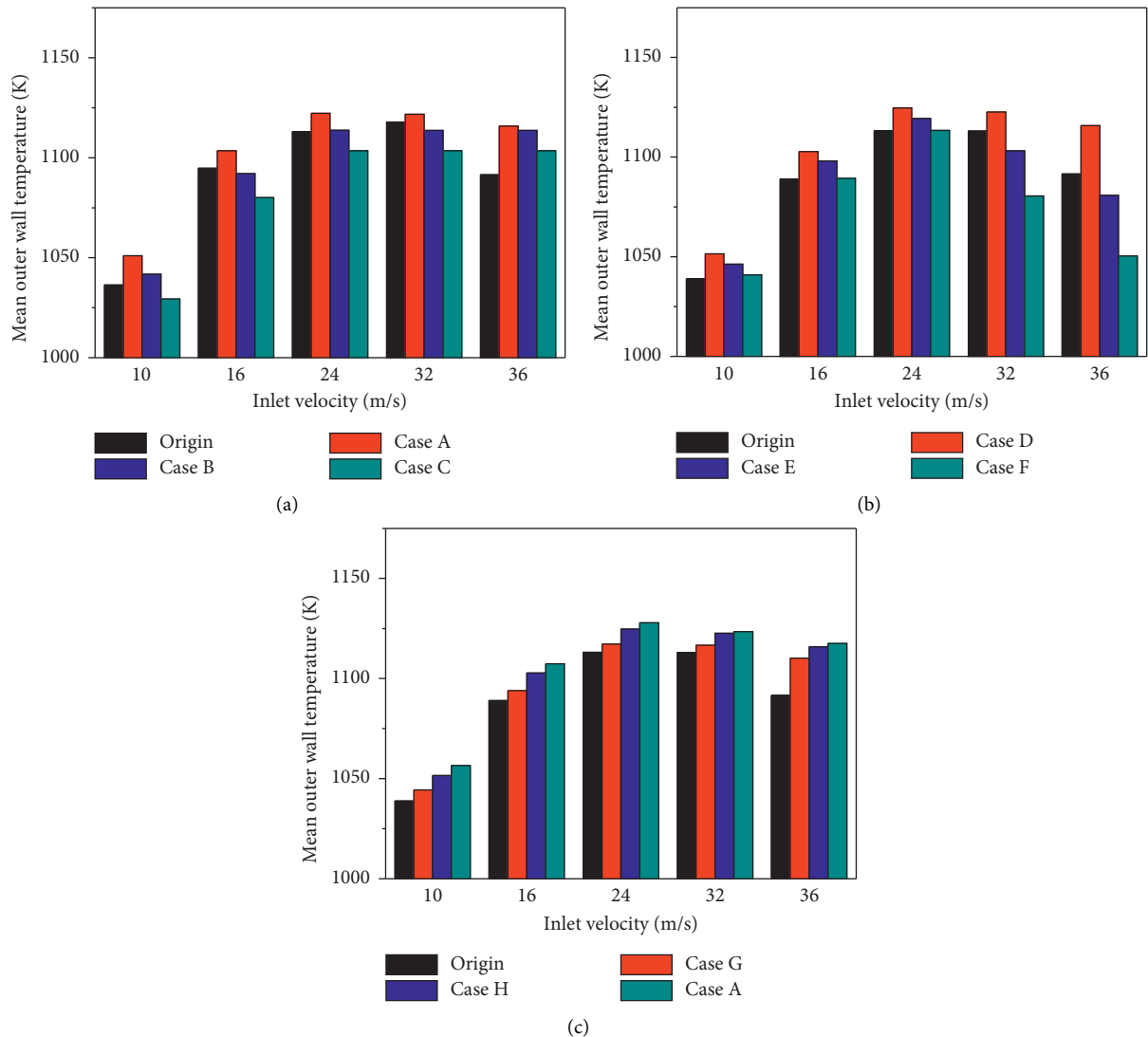


FIGURE 7: Average wall temperature versus inlet velocity for the combustor under $\Phi=0.4$.

resistance in the horizontal direction caused by the thinning of the outer wall of the cavity. Moreover, the combustion chamber with H equal to 0.75 mm has the highest mean wall temperature, followed by that with H equals 0.5 mm, 0.25 mm, and the original combustion chamber (Figure 7(c)). This phenomenon occurs because the high rib height enlarges the area of the recirculation and low-velocity zones, thereby prolonging the residence time of the mixture and boosting the heat transfer between the mixture and wall.

Figure 8 presents the radical OH distribution of the original and improved microcombustion chambers. Accordingly, the equivalence ratio and inlet velocity are maintained at 0.4 and 10 m/s, respectively. Figure 8 shows that when the inlet velocity equals 10 m/s, the highest mass fractions of OH in the microcombustors are approximately identical. The reaction zone is mainly located in the cavities of the original combustor. Low-velocity and recirculation zones are formed in the cavities, which anchor the flame and provide a high local temperature and an improved heat

recirculation region. In addition, the OH concentration in the boundary layer in the combustion chamber of $L_3=1.25$ mm, $H=0.75$ mm, and $L_4=1.25$ mm is higher than those of the original combustion chamber. Given the increase in the upstream and downstream step lengths, the OH concentration in the boundary layer decreases. In addition, the OH concentration in the boundary layer increases with the increase in rib height because the wall temperature level also increases, thereby substantially preheating the mixture and enhancing the reaction intensity.

Figure 9 presents the temperature distribution for different microcombustors, in which the equivalence ratio and inlet velocity are maintained at 0.4 and 10 m/s, respectively. The variation in high-temperature regions is consistent with that in the reaction zones, as demonstrated by the comparison shown in Figure 8. The highest wall temperature zone is near the downstream of the cavities. The outer wall temperature levels of the improved microcombustor are higher than that of the original microcombustor. As the

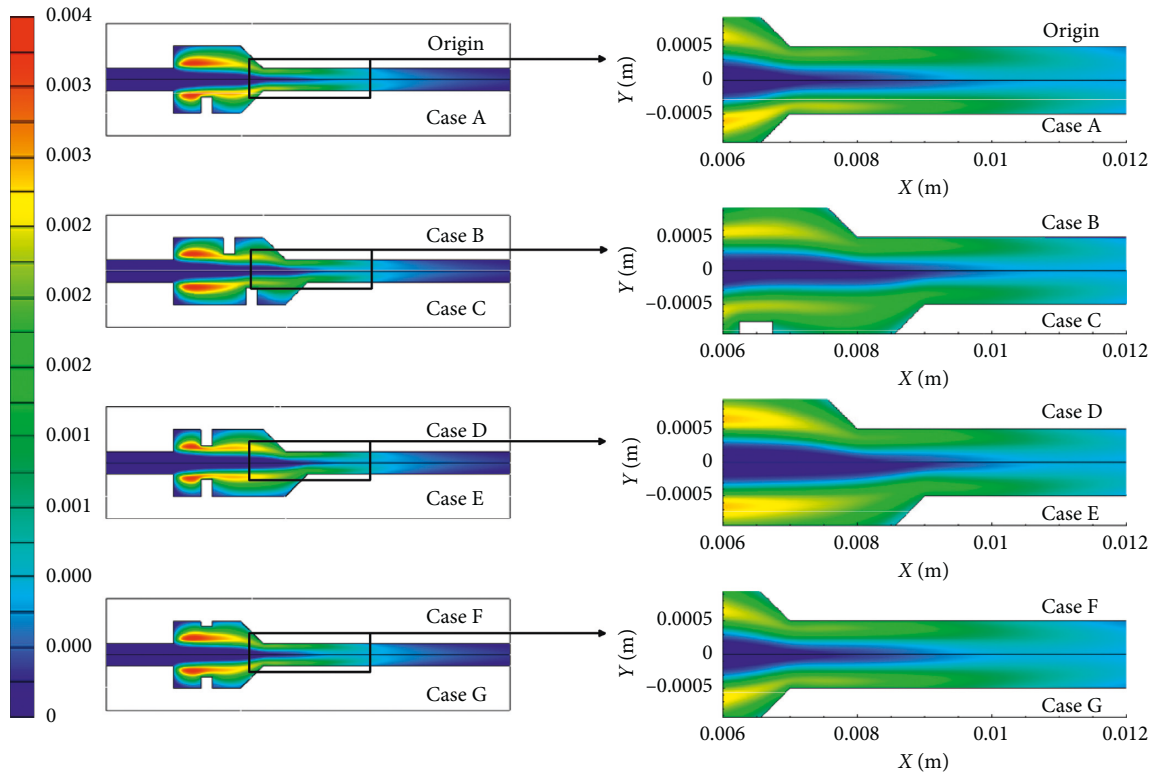


FIGURE 8: Mass fraction contours of OH in the different combustor; the inlet velocity is 10 m/s.

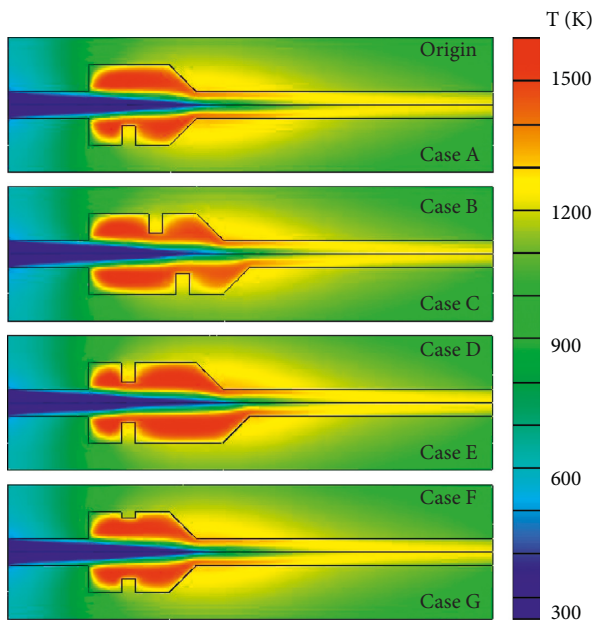


FIGURE 9: Temperature distribution in the different combustor; the inlet velocity is 10 m/s.

upstream and downstream step lengths increase, the area of the high-temperature zone and temperature level near the cavities decrease correspondingly.

Figure 10 presents the radical H_2 distribution of the original and improved microcombustion chambers. Compared with that of the original combustor, hydrogen

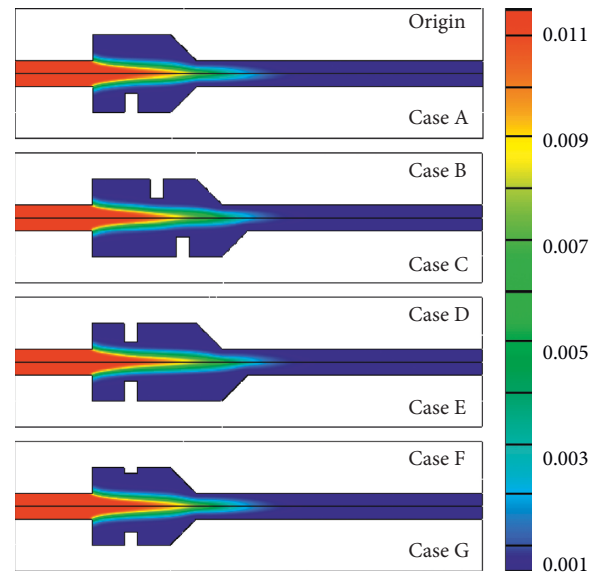


FIGURE 10: Radical H_2 distribution in the different combustors; inlet velocity is 10 m/s.

has a longer consume distance. Moreover, the hydrogen consumes distance increased with the step length. The combustor also has a considerably short hydrogen consume distance with the rib height raised. The combustion chamber of $L_3=1.25$ mm, $H=0.75$ mm, and $L_4=1.25$ mm has the shortest hydrogen consume distance compared with those of other improved combustion chambers.

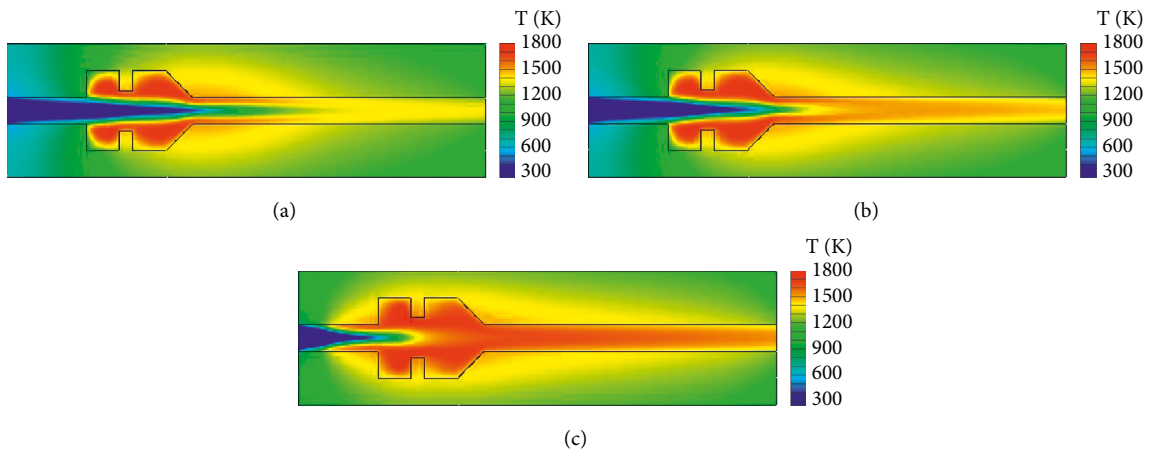


FIGURE 11: Temperature distribution of the improved microcombustor at equivalence ratios: (a) $\Phi = 0.4$, (b) $\Phi = 0.5$, and (c) $\Phi = 0.6$.

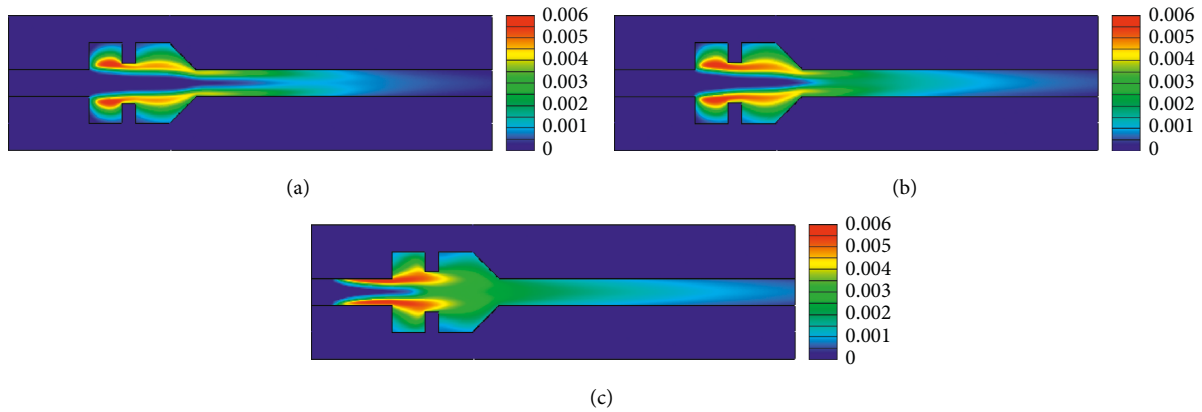


FIGURE 12: OH distribution of the improved microcombustor at equivalence ratios: (a) $\Phi = 0.4$, (b) $\Phi = 0.5$, and (c) $\Phi = 0.6$.

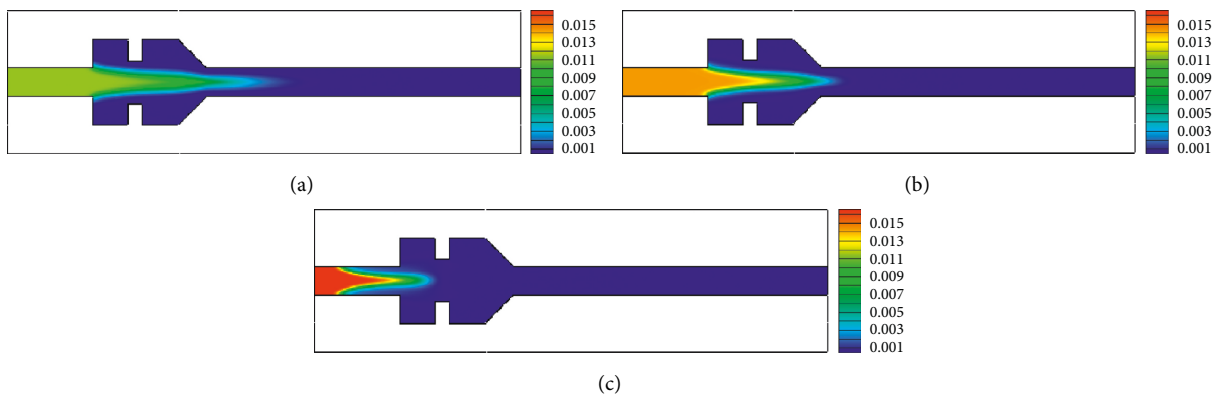


FIGURE 13: H_2 distribution of the improved microcombustor at the following equivalence ratios: (a) $\Phi = 0.4$, (b) $\Phi = 0.5$, and (c) $\Phi = 0.6$.

3.2. Effects of Equivalence Ratio on Combustion Performances of Microcombustors with Rectangular Ribs. Figure 11 shows the contours of the temperature distributions for the microcombustor with the upstream and downstream step lengths and rib height equal to 1.25, 1.25, and 0.75 mm, respectively, under various equivalence ratios. The inlet velocities are maintained at 10 m/s. The temperature levels in the cavities increase as the equivalence ratio is boosted.

This increase indicates that the chemical reaction becomes intensive at large equivalence ratios (Figure 12). When the equivalence ratio is below 0.5, the main reaction zone is located in the cavities. With further increase of the equivalence ratio, the flame front moved upstream in the combustor as the equivalence ratio equals 0.6.

Figure 13 shows the contours of the H_2 distributions for the microcombustor with the upstream and downstream

step lengths and rib height equal to 1.25, 1.25, and 0.75 mm, respectively, under various equivalence ratios. The inlet velocities are maintained at 10 m/s. The hydrogen consumes distance in the combustor decreased with an increase in the equivalence ratio. As the equivalence ratio equals 0.6, hydrogen is consumed completely before the cavities, which means rapid burning speed.

4. Conclusions

This study designed a microcombustion chamber with a rectangular rib. The effects of the step length and rib height on the premixed H₂/air combustion were numerically investigated. The performance of the original design was compared with that of the newly proposed designs under different inlet velocities.

The results show that the new design improves the outer wall temperature profile for the thermoelectric and thermophotovoltaic devices. This outcome occurs because the recirculation and low-velocity zone areas of the improved microcombustion chamber are equal to or above those of the combustor without the rectangular rib. Consequently, the heat transfer between the mixture and the wall is enhanced by the rectangular rib. Moreover, the flow field is not the sole factor that influences wall temperature level because the outer wall profile and average wall temperature of the combustor decrease with step length. This situation is due to the increase in the thermal resistance in the horizontal direction because of the thinning of the outer wall of the cavity, thereby resulting in low heat being conducted upstream through the thin outer wall with a large step length; hence, the upstream and downstream step lengths and rib height equal to 1.25, 1.25, and 0.75 mm microcombustor is recommended due to the higher outer wall temperature and average wall temperature. Moreover, when the equivalence ratio is extremely high (e.g., 0.6), the combustion chamber wall temperature has exceeded the tolerable temperature of the quartz.

A sufficiently high combustor wall temperature level is desired for thermoelectric and thermophotovoltaic devices. Thus, the improved microcombustor is recommended.

Data Availability

The numerical data used to support the findings of this study are included within the article.

Additional Points

Highlights. (1) A microcombustor with an improved rib is proposed. (2) The working performance of combustors with various step lengths and rib height is studied. (3) The combustion performances of the original and improved combustors are compared.

Conflicts of Interest

The authors declare that they have no conflicts of interest.

References

- [1] S. Meziane and A. Bentebbiche, "Numerical study of blended fuel natural gas-hydrogen combustion in rich/quench/lean combustor of a micro gas turbine," *International Journal of Hydrogen Energy*, vol. 44, no. 29, pp. 15610–15621, 2019.
- [2] Q. Peng, W. Yang, E. Jiaqiang et al., "Experimental investigation on premixed hydrogen/air combustion in varied size combustors inserted with porous medium for thermophotovoltaic system applications," *Energy Conversion and Management*, vol. 200, 2019.
- [3] Y. Yan, G. Wu, W. Huang, L. Zhang, L. Li, and Z. Yang, "Numerical comparison study of methane catalytic combustion characteristic between newly proposed opposed counter-flow micro-combustor and the conventional ones," *Energy*, vol. 170, pp. 403–410, 2019.
- [4] Q. Peng, E. Jiaqiang, W. M. Yang et al., "Effects analysis on combustion and thermal performance enhancement of a nozzle-inlet micro tube fueled by the premixed hydrogen/air," *Energy*, vol. 160, pp. 349–360, 2018.
- [5] J. Pan, J. Zhu, Q. Liu, Y. Zhu, A. Tang, and Q. Lu, "Effect of micro-pin-fin arrays on the heat transfer and combustion characteristics in the micro-combustor," *International Journal of Hydrogen Energy*, vol. 42, no. 36, pp. 23207–23217, 2017.
- [6] Q. Peng, Y. Wu, E. Jiaqiang, W. Yang, H. Xu, and Z. Li, "Combustion characteristics and thermal performance of premixed hydrogen-air in a two-rearward-step micro tube," *Applied Energy*, vol. 242, pp. 424–438, 2019.
- [7] G. Wu, Z. Lu, W. Pan, Y. Guan, S. Li, and C. Z. Ji, "Experimental demonstration of mitigating self-excited combustion oscillations using an electrical heater," *Applied Energy*, vol. 239, pp. 331–342, 2019.
- [8] Q. Peng, E. Jiaqiang, W. M. Yang et al., "Experimental and numerical investigation of a micro-thermophotovoltaic system with different backward-facing steps and wall thicknesses," *Energy*, vol. 173, pp. 540–547, 2019.
- [9] Y. Yan, Z. Zhang, L. Zhang, X. Wang, K. Liu, and Z. Yang, "Investigation of autothermal reforming of methane for hydrogen production in a spiral multi-cylinder micro-reactor used for mobile fuel cell," *International Journal of Hydrogen Energy*, vol. 40, no. 4, pp. 1886–1893, 2015.
- [10] R. Wang, J. Ran, X. Du, J. Niu, and W. Qi, "The influence of slight protuberances in a micro-tube reactor on methane/moist air catalytic combustion," *Energies*, vol. 9, no. 6, p. 421, 2016.
- [11] P. Zhang, R. Jing-yu, Z. Zhang, X. Du, W. Qi, and J. Niu, "Investigation on the effect of water vapor on the catalytic combustion of methane on platinum," *Petroleum Science & Technology*, vol. 36, no. 7, pp. 494–499, 2018.
- [12] Q. Peng, E. Jiaqiang, Z. Zhang, W. Hu, and X. Zhao, "Investigation on the effects of front-cavity on flame location and thermal performance of a cylindrical micro combustor," *Applied Thermal Engineering*, vol. 130, pp. 541–551, 2018.
- [13] J. Wan, A. Fan, H. Yao, and W. Liu, "Effect of thermal conductivity of solid wall on combustion efficiency of a micro-combustor with cavities," *Energy Conversion and Management*, vol. 96, pp. 605–612, 2015.
- [14] J. Wan, A. Fan, H. Yao, and W. Liu, "Flame-anchoring mechanisms of a micro cavity-combustor for premixed H₂/air flame," *Chemical Engineering Journal*, vol. 275, pp. 17–26, 2015.
- [15] W. Yang, Y. Xiang, A. Fan, and H. Yao, "Effect of the cavity depth on the combustion efficiency of lean H₂/air flames in a

- micro combustor with dual cavities,” *International Journal of Hydrogen Energy*, vol. 42, no. 20, pp. 14312–14320, 2017.
- [16] J. Wan and A. Fan, “Effect of channel gap distance on the flame blow-off limit in mesoscale channels with cavities for premixed CH₄/air flames,” *Chemical Engineering Science*, vol. 132, pp. 99–107, 2015.
- [17] G. Bagheri, S. Ehsan Hosseini, and M. Abdul Wahid, “Effects of bluff body shape on the flame stability in premixed micro-combustion of hydrogen-air mixture,” *Applied Thermal Engineering*, vol. 67, no. 1-2, pp. 266–272, 2014.
- [18] E. Jiaqiang, H. Liu, X. Zhao et al., “Investigation on the combustion performance enhancement of the premixed methane/air in a two-step micro combustor,” *Applied Thermal Engineering*, vol. 141, pp. 114–125, 2018.
- [19] W. Zuo, E. Jiaqiang, H. Liu, Q. Peng, X. Zhao, and Z. Zhang, “Numerical investigations on an improved micro-cylindrical combustor with rectangular rib for enhancing heat transfer,” *Applied Energy*, vol. 184, pp. 77–87, 2016.
- [20] J. Wan, A. Fan, and H. Yao, “Effect of the length of a plate flame holder on flame blowout limit in a micro-combustor with preheating channels,” *Combustion and Flame*, vol. 170, pp. 53–62, 2016.
- [21] E. Jiaqiang, Q. Peng, X. Zhao, W. Zuo, Z. Zhang, and M. Pham, “Numerical investigation on the combustion characteristics of non-premixed hydrogen-air in a novel micro-combustor,” *Applied Thermal Engineering*, vol. 110, pp. 665–677, 2017.
- [22] H. Yilmaz, O. Cam, and I. Yilmaz, “Effect of micro combustor geometry on combustion and emission behavior of premixed hydrogen/air flames,” *Energy*, vol. 135, pp. 585–597, 2017.
- [23] I. Yilmaz, H. Yilmaz, O. Cam, and M. Ilbas, “Combustion characteristics of premixed hydrogen/air flames in a geometrically modified micro combustor,” *Fuel*, vol. 217, pp. 536–543, 2018.
- [24] W. Zuo, E. Jiaqiang, and R. Lin, “Numerical investigations on an improved counterflow double-channel micro combustor fueled with hydrogen for enhancing thermal performance,” *Energy Conversion and Management*, vol. 159, pp. 163–174, 2018.
- [25] Y.-f. Yan, H.-y. Yan, L. Zhang, L. Li, J. Zhu, and Z. Zhang, “Numerical investigation on combustion characteristics of methane/air in a micro-combustor with a regular triangular pyramid bluff body,” *International Journal of Hydrogen Energy*, vol. 43, no. 15, 2018.
- [26] M. Ansari and E. Amani, “Micro-combustor performance enhancement using a novel combined baffle-bluff configuration,” *Chemical Engineering Science*, vol. 175, pp. 243–256, 2018.
- [27] L. Li, Z. Yuan, Y. Xiang, and A. Fan, “Numerical investigation on mixing performance and diffusion combustion characteristics of H₂ and air in planar micro-combustor,” *International Journal of Hydrogen Energy*, vol. 43, no. 27, pp. 12491–12498, 2018.
- [28] A. Tang, J. Deng, Y. Xu, J. Pan, and T. Cai, “Experimental and numerical study of premixed propane/air combustion in the micro-planar combustor with a cross-plate insert,” *Applied Thermal Engineering*, vol. 136, pp. 177–184, 2018.
- [29] W. Zuo, E. Jiaqiang, W. Hu, Y. Jin, and D. Han, “Numerical investigations on combustion characteristics of H₂/air premixed combustion in a micro elliptical tube combustor,” *Energy*, vol. 126, pp. 1–12, 2017.
- [30] S. Akhtar, M. N. Khan, J. C. Kurnia, and T. Shamim, “Investigation of energy conversion and flame stability in a curved micro-combustor for thermo-photovoltaic (TPV) applications,” *Applied Energy*, vol. 192, pp. 134–145, 2017.
- [31] B. Aravind, G. K. S. Raghuram, V. R. Kishore, and S. Kumar, “Compact design of planar stepped micro combustor for portable thermoelectric power generation,” *Energy Conversion and Management*, vol. 156, pp. 224–234, 2018.
- [32] Y.-H. Li and J.-R. Hong, “Performance assessment of catalytic combustion-driven thermophotovoltaic platinum tubular reactor,” *Applied Energy*, vol. 211, pp. 843–853, 2018.
- [33] Y. Yan, W. Huang, W. Tang et al., “Numerical study on catalytic combustion and extinction characteristics of premixed methane-air in micro flatbed channel under different parameters of operation and wall,” *Fuel*, vol. 180, pp. 659–667, 2016.
- [34] J. Ran, L. Li, X. Du, R. Wang, W. Pan, and W. Tang, “Numerical investigations on characteristics of methane catalytic combustion in micro-channels with a concave or convex wall cavity,” *Energy Conversion and Management*, vol. 97, pp. 188–195, 2015.
- [35] C. Luo, Y. Li, Z. Liu, and Y. Dong, “Catalytic combustion of low concentration methane in micro-combustor,” *CIESC Journal*, vol. 66, pp. 216–221, 2015.
- [36] J. Pan, R. Zhang, Q. Lu, Z. Zha, and S. Bani, “Experimental study on premixed methane-air catalytic combustion in rectangular micro channel,” *Applied Thermal Engineering*, vol. 117, pp. 1–7, 2017.
- [37] J. M. Rodrigues, M. F. Ribeiro, and E. C. Fernandes, “Catalytic activity of electrodeposited cobalt oxide films for methane combustion in a micro-channel reactor,” *Fuel*, vol. 232, pp. 51–59, 2018.
- [38] Y. Wang, J. Zhou, Q. Zhao, W. Yang, J. Zhou, and Y. Zhang, “Comparison of catalytic combustion of methane and n-butane in microtube,” *CIESC Journal*, vol. 68, pp. 896–902, 2017.
- [39] C. H. Kuo and P. D. Ronney, “Numerical modeling of non-adiabatic heat-recirculating combustors,” *Proceedings of the Combustion Institute*, vol. 31, no. 2, pp. 3277–3284, 2007.
- [40] J. Li, Z. Zhao, A. Kazakov, and F. L. Dryer, “An updated comprehensive kinetic model of hydrogen combustion,” *International Journal of Chemical Kinetics*, vol. 36, no. 10, pp. 566–575, 2004.
- [41] J. Wan, W. Yang, A. Fan et al., “A numerical investigation on combustion characteristics of H₂/air mixture in a micro-combustor with wall cavities,” *International Journal of Hydrogen Energy*, vol. 39, no. 15, pp. 8138–8146, 2014.



Hindawi

Submit your manuscripts at
www.hindawi.com

